

# CARBON BURNING - HYDROSTATIC

## WHERE?

- **MASSIVE STARS**

C core burning following  
He-burning & before Ne-b'g

- **SUPER AGB STARS**

C-O core collapses & burns  
to O-Ne and degenerate elec.

## WHERE NOT?

- **LOW & INTERMEDIATE MASS AGB \*S**

C-O core supported by  
degenerate electrons

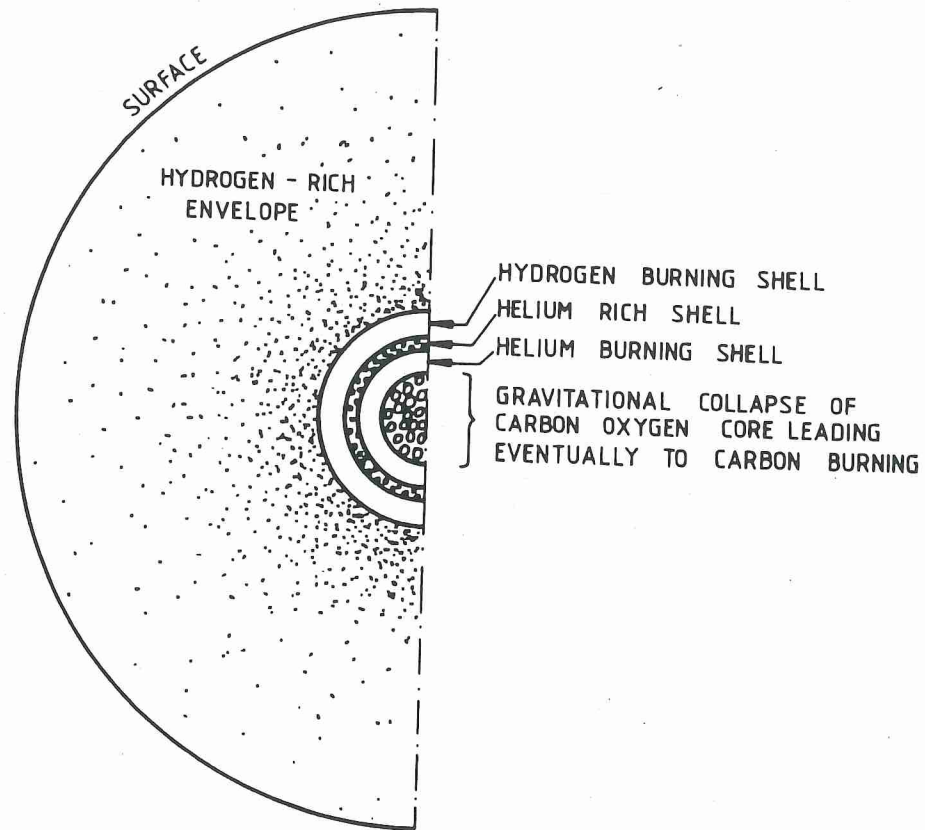
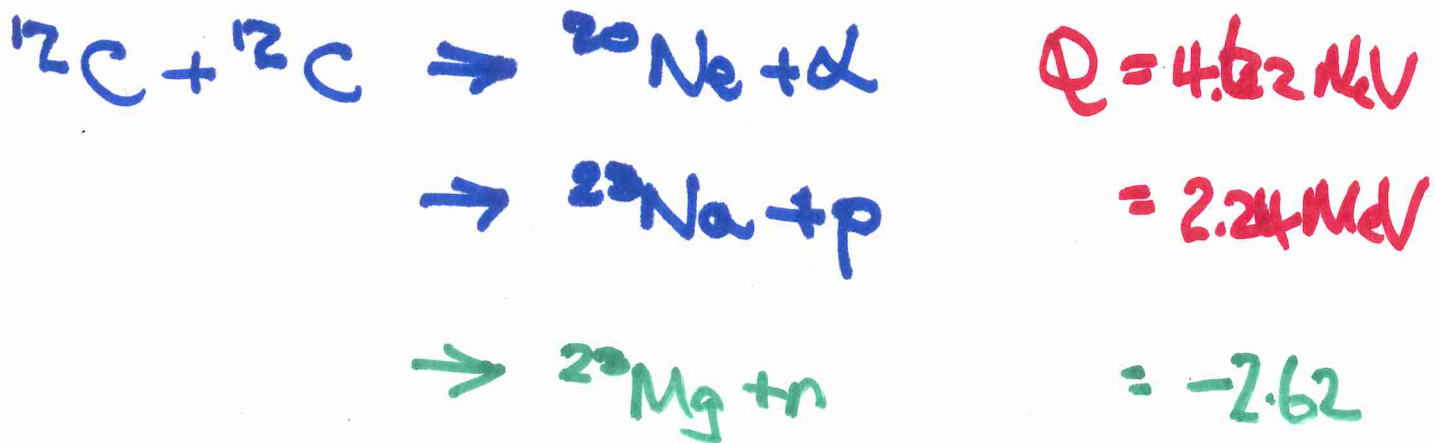


FIGURE 8.1. Schematic showing the cross-sectional view of a massive star ( $M \geq 8 M_{\odot}$ ) after the helium fuel in the core is depleted. At this stage, helium and hydrogen burning continue in concentric shells around the contracting carbon-oxygen core. Contraction of the core eventually triggers the burning of carbon, and the gravitational collapse stops.

## C BURNING SUMMARY



at  $T_6 \sim 500$  and  $\rho \sim 3 \times 10^6 \text{ g/cm}^3$

- $\sigma$  via COMPOUND NUCLEUS  
(CAULDRONS Fig 8.2)
- NEUTRINO LOSSES and smaller  
 $\Delta E = \Delta m c^2 \rightarrow$  SHORT timescale
- PRINCIPAL PRODUCTS  
 ${}^{20}\text{Ne}$ ,  ${}^{24}\text{Mg}$ ,  ${}^{23}\text{Na}$
- MINOR PRODUCTS via p, n,  $\alpha$ 's
- SOME CONSUMPTION of  ${}^{16}\text{O}$

# HEAVY - ION BURNING IN STARS

EXAMPLE : CARBON BURNING  $^{12}\text{C} + ^{12}\text{C}$

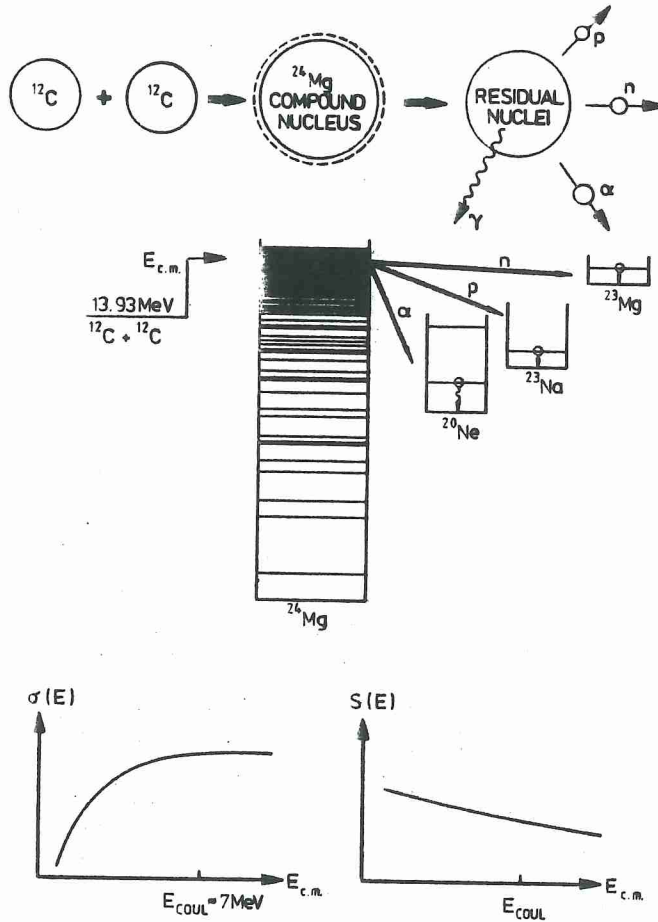
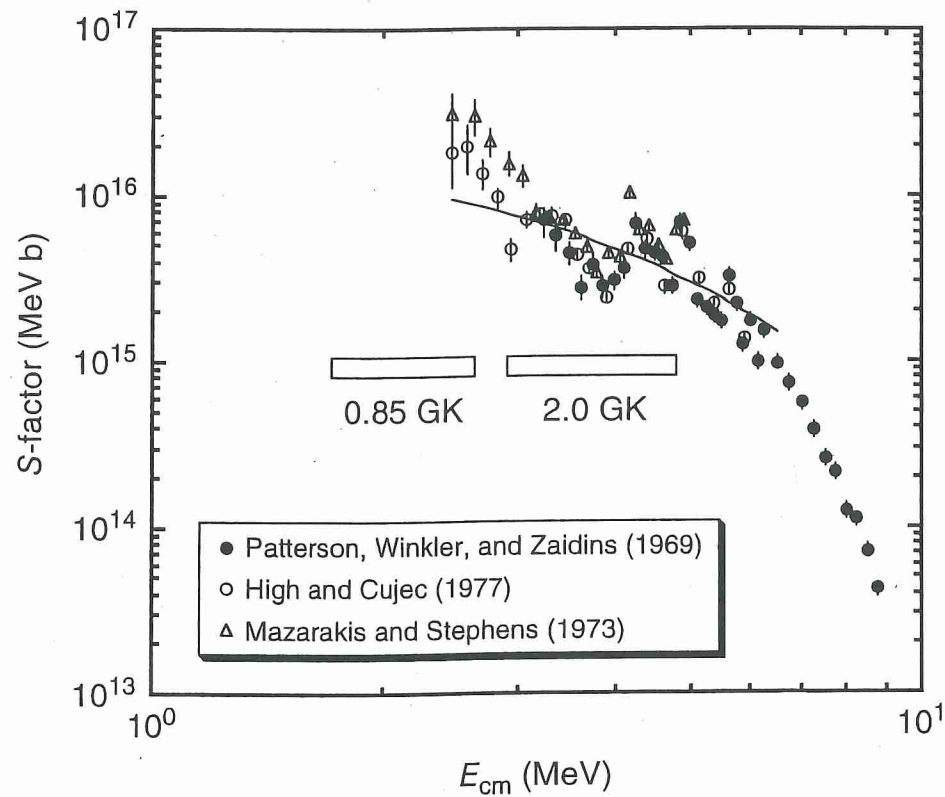
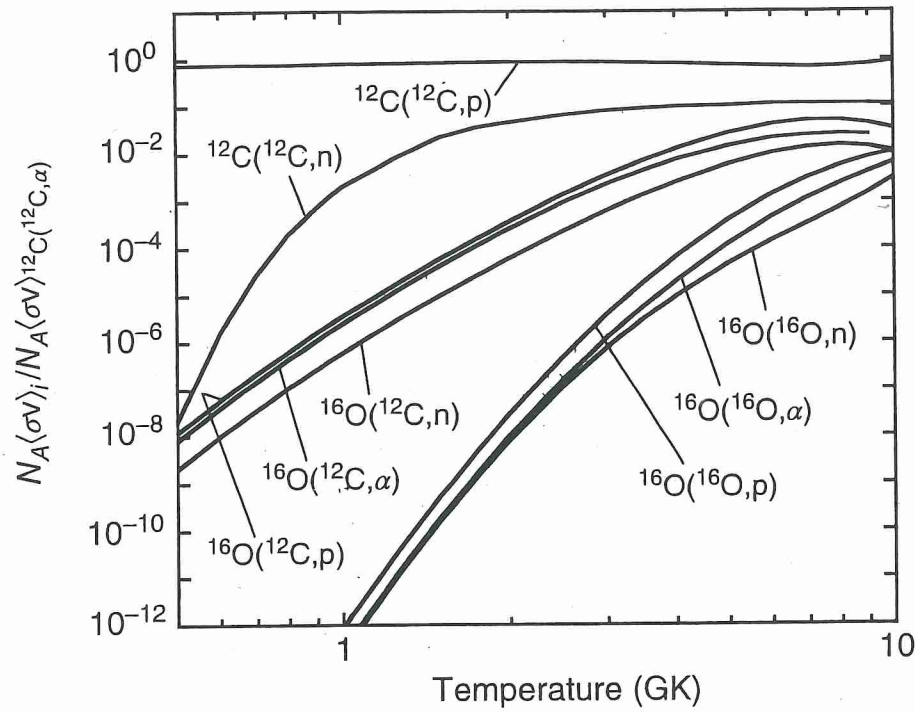


FIGURE 8.2. The heavy-ion reactions such as  $^{12}\text{C} + ^{12}\text{C}$  proceed through compound nuclei at high excitation energies, where the level density is high and the states overlap appreciably. As a result the cross section and the S-factor should vary smoothly with energy. The reaction can be studied either by detecting the light particles evaporated from the compound nucleus or the  $\gamma$ -rays emitted from the residual nuclei. Direct detection of the recoil nuclei is difficult and has to date not been performed at low interaction energies (chap. 5).



**Figure 5.24** Total S-factor for the  $^{12}\text{C} + ^{12}\text{C}$  reaction. The data are adopted from Patterson, Winkler, and Zaidins (1969), Mazarakis and Stephens (1973), and High and Cujec (1977). The data of Becker *et al.* (1981) are not shown. The open bars indicate the location of the Gamow peaks for  $T \approx 0.85$  GK

(core carbon burning) and  $T \approx 2.0$  GK (explosive carbon burning). The origin of the strong fluctuation in the S-factor (or cross section) remains obscure. The solid line shows the fitted total S-factor adopted by Caughlan and Fowler (1988).



**Figure 5.25** Reaction rates for various  $^{12}\text{C} + ^{12}\text{C}$ ,  $^{12}\text{C} + ^{16}\text{O}$ , and  $^{16}\text{O} + ^{16}\text{O}$  reaction channels. From Caughlan and Fowler (1988); Dayras, Switkowski, and Woosley (1977). For

better comparison, the  $N_A\langle\sigma v\rangle$  values are given relative to the  $^{12}\text{C}(^{12}\text{C},\alpha)^{20}\text{Ne}$  reaction rate. The displayed results disregard electron screening corrections.

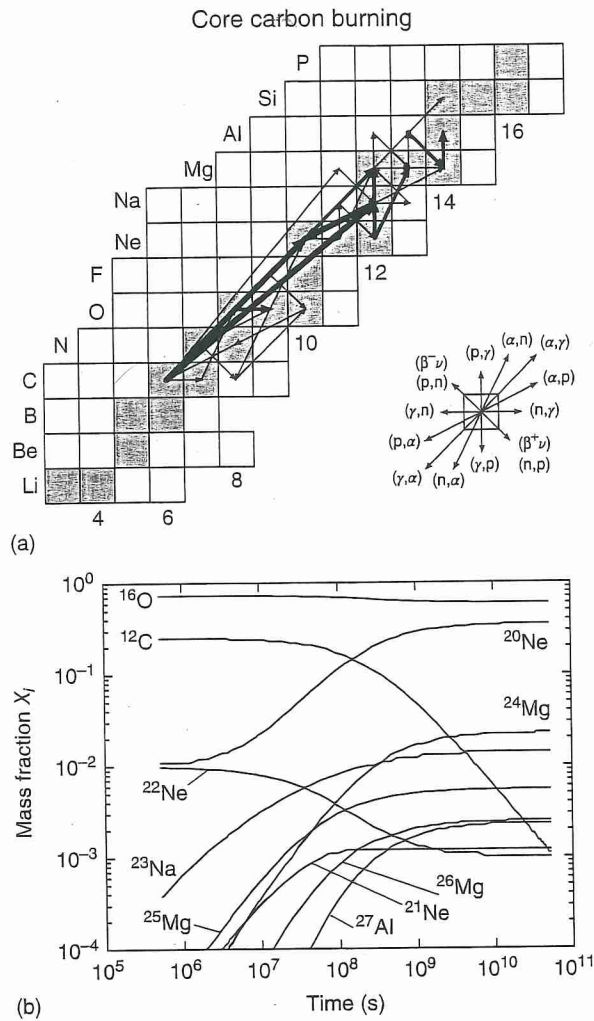


**Figure 5.26** (a) Time-integrated net abundance flows, and (b) abundance evolutions for a constant temperature and density of  $T = 0.9 \text{ GK}$  and  $\rho = 10^5 \text{ g/cm}^3$ , respectively. Such conditions are typical of core carbon burning in stars with an initial mass of  $M = 25 M_{\odot}$  and with initial solar metallicity. The reaction network is solved numerically until the carbon fuel is exhausted ( $X_{12\text{C}} < 10^{-3}$  after  $\approx 1600 \text{ y}$ ). Arrows represent net (forward minus reverse) abundance flows, integrated over the entire computation time. The magnitude of the abundance flows is represented

by arrows of three different thicknesses:  $F_{ij}^{\text{max}} \geq F_{ij} > 0.1 F_{ij}^{\text{max}}$  (thick arrows),  $0.1 F_{ij}^{\text{max}} \geq F_{ij} > 0.01 F_{ij}^{\text{max}}$  (intermediate arrows), and  $0.01 F_{ij}^{\text{max}} \geq F_{ij} > 0.001 F_{ij}^{\text{max}}$  (thin arrows), where  $F_{ij}^{\text{max}}$  corresponds to the reaction with the maximum net flow. Shaded squares indicate stable isotopes. A particular nuclide can be identified from the element symbol (vertical axis) and neutron number (horizontal axis). The key (middle right) indicates the correspondence between abundance flow arrow direction and reaction type. The  $^{16}\text{O}(\alpha, \gamma)^{20}\text{Ne}$  reaction is obscured by  $^{12}\text{C}(^{12}\text{C}, \alpha)^{20}\text{Ne}$  in part (a).

# NEON BURNING : MASSIVE STARS

• PRIMARILY:  $^{20}\text{Ne} (\gamma, \alpha) ^{16}\text{O}$

$\alpha$ -SEPARATION ENERGY 'ONLY'

4.73 MeV &  $T_6 \sim 1700 \rightarrow$

LOTS OF 5 MeV PHOTONS

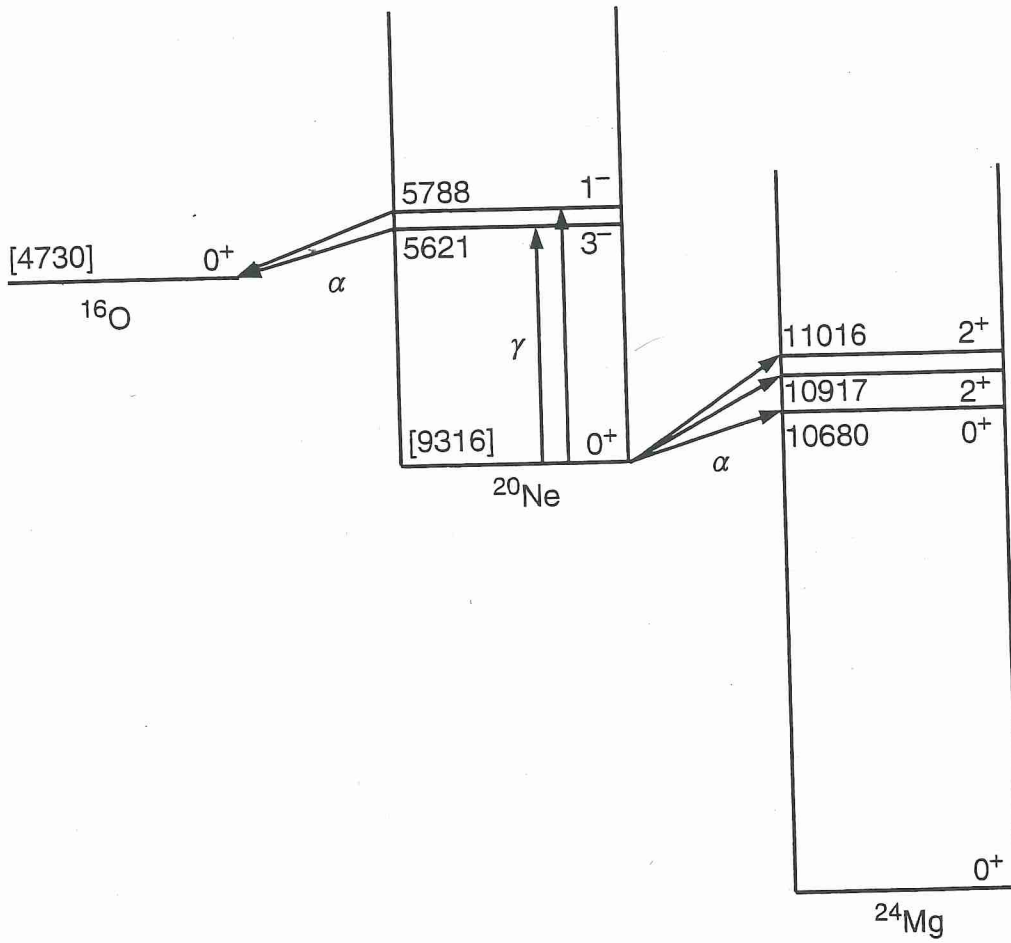
• SECONDARILY:

$^{20}\text{Ne} (\alpha, \gamma) ^{24}\text{Mg} (\alpha, \gamma) ^{28}\text{Si}$

$^{23}\text{Ne} (\alpha, p) ^{26}\text{Mg} (\alpha, n) ^{29}\text{Si}$

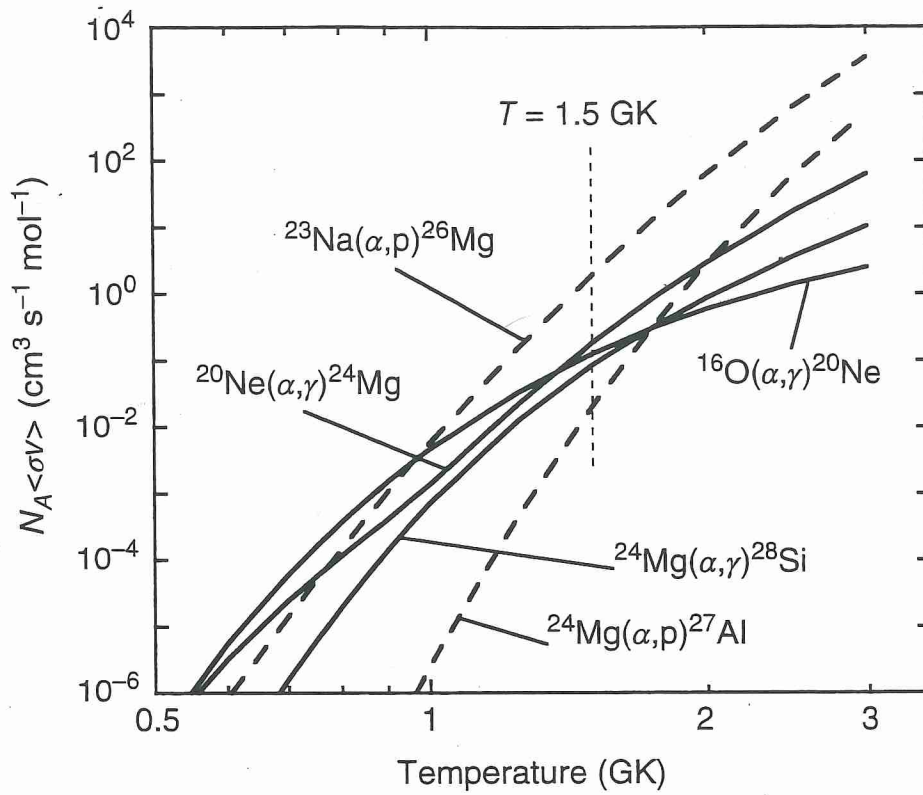
+ . . . . .





**Figure 5.28** Energy level diagrams for the most important nuclides participating in neon burning. Numbers in square brackets represent reaction  $Q$ -values (Wang *et al.* 2012; see also caption to Figure 5.21).

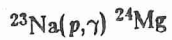
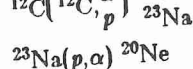
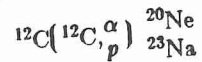
Excitation energies and quantum numbers are from Tilley *et al.* (1998) and Endt (1990). Levels that are not important for neon burning are omitted.



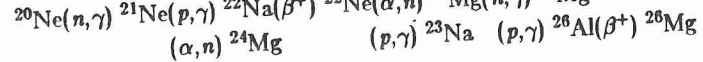
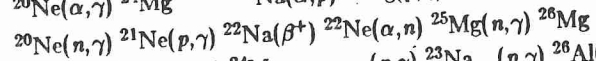
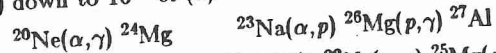
**Figure 5.27** Rates for  $\alpha$ -particle-induced reactions on  $^{16}\text{O}$ ,  $^{20}\text{Ne}$ ,  $^{23}\text{Na}$ , and  $^{24}\text{Mg}$  versus temperature. The vertical dashed line indicates a temperature of  $T = 1.5$  GK typical for core neon burning in massive stars.

Table 11.4  
Important Reactions in Carbon Burning

(a) basic reactions



(b) down to  $10^{-2}$  of (a)



(c) low temperature, high density

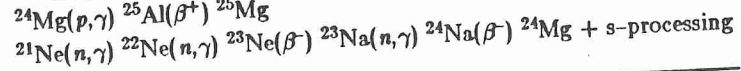
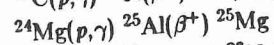
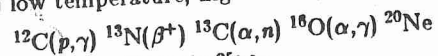
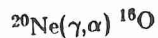
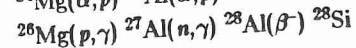
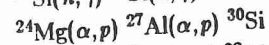
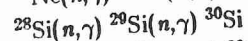
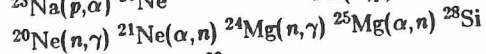
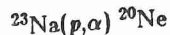


Table 11.5  
Neon Burning

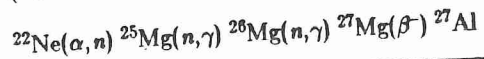
(a) basic reactions



(b) flows  $> 10^{-2} \times$  (a)



(c) at low temperature and high density  
( $^{22}\text{Ne}$  left from prior n-rich C-burning)



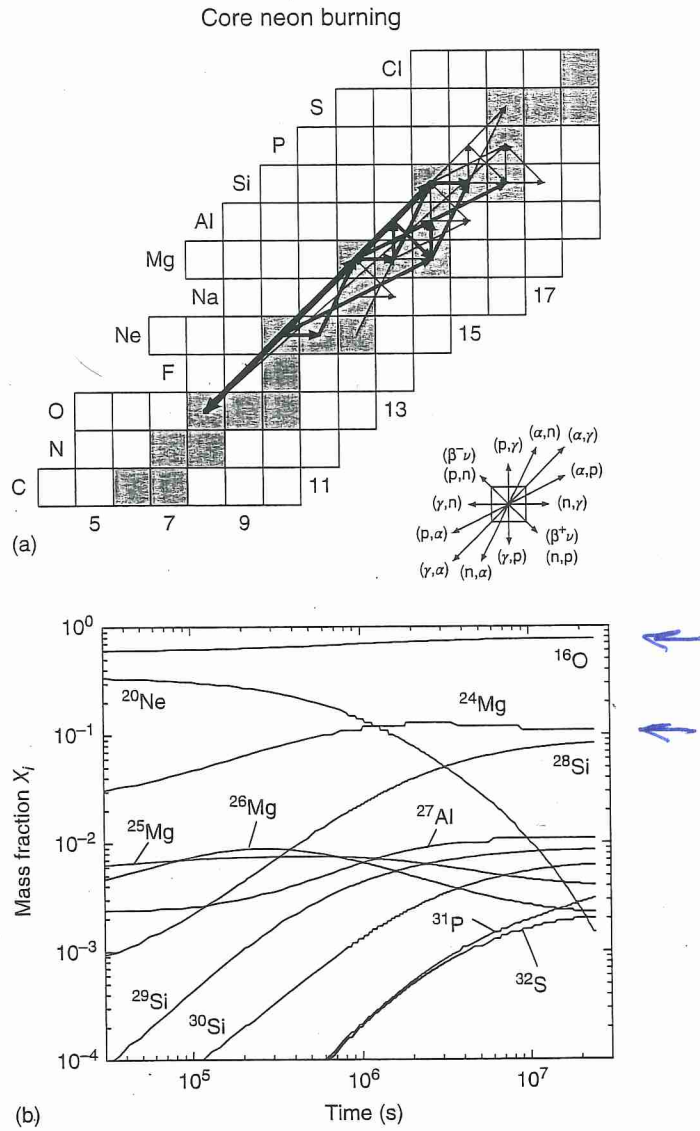
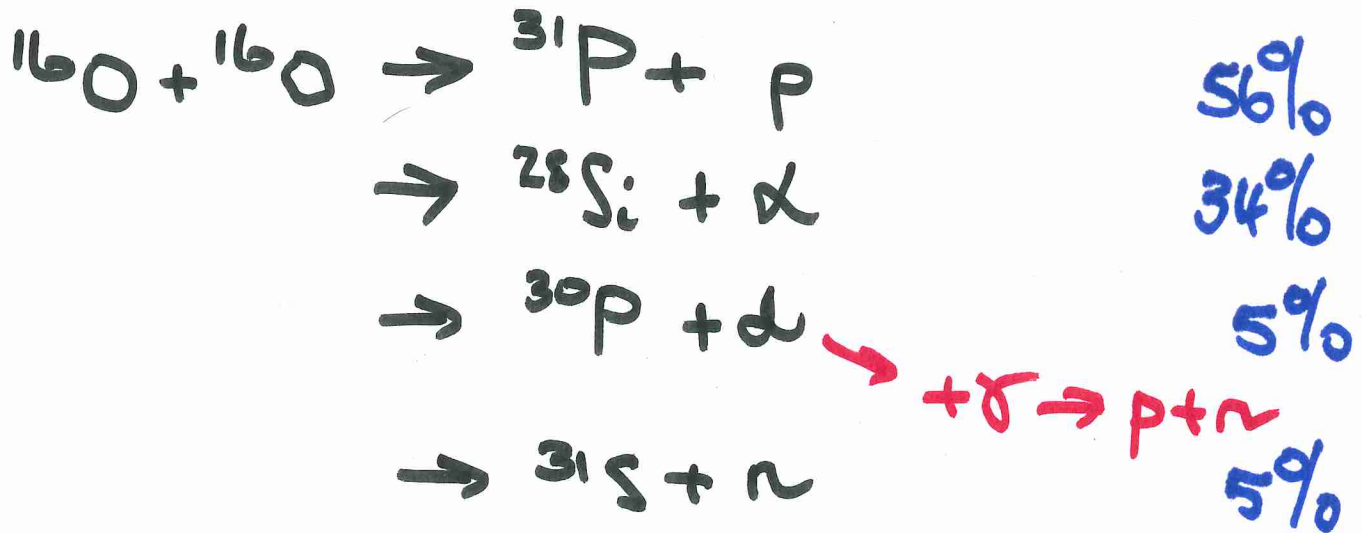


**Figure 5.29** (a) Time-integrated net abundance flows, and (b) abundance evolutions for a constant temperature and density of  $T = 1.5$  GK and  $\rho = 5 \times 10^6$  g/cm<sup>3</sup>, respectively. Such conditions are typical of core neon burning in stars with an initial mass of  $M = 25 M_{\odot}$  and with initial solar metallicity. The reaction network is solved numerically until the neon fuel is exhausted ( $X_{20\text{Ne}} < 0.0015$  after  $\approx 280$  d). The arrows, shaded squares, and key in the top part have the same meaning as in Figure 5.26.

# OXYGEN BURNING - MASSIVE STARS

PRIMARYLY:



also  ${}^{16}\text{O}(\gamma, \alpha){}^{12}\text{C}$

SECONDARILY: p, n,  $\alpha$  reactions

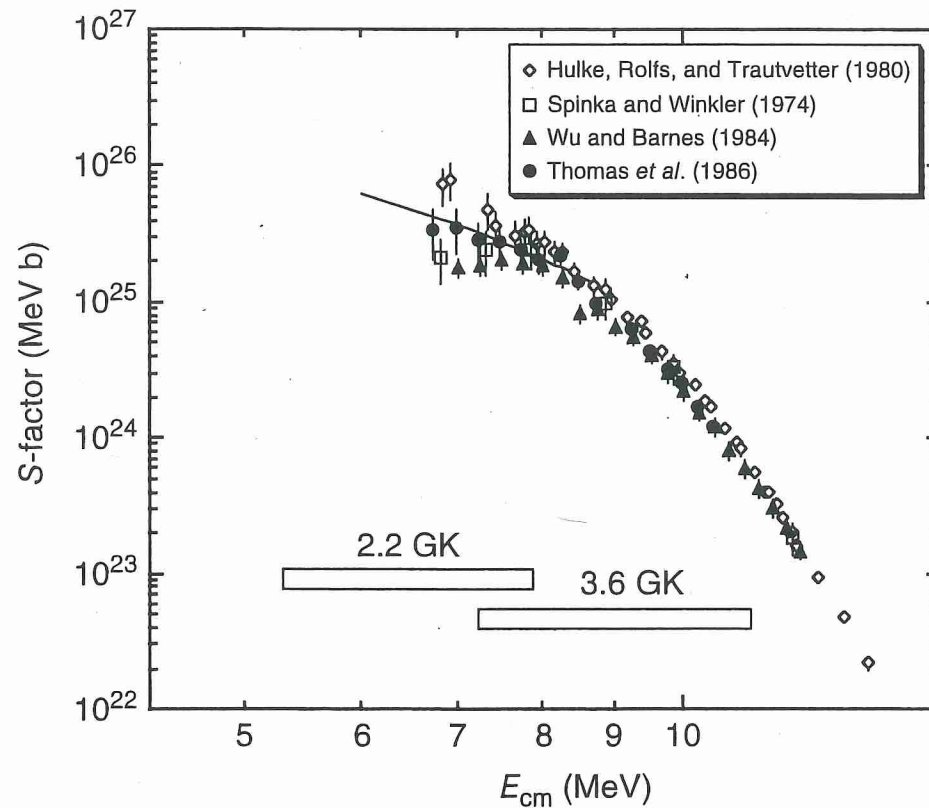


**Figure 5.31** Total  $S$ -factor for the  $^{16}\text{O} + ^{16}\text{O}$  reaction. The data are adopted from Spinka and Winkler (1974), Hulke, Rolfs, and Trautvetter (1980), Wu and Barnes (1984), and Thomas *et al.* (1986). The data from Thomas *et al.* (1986) are extracted from their

Figures 9 and 10. The open bars indicate the location of the Gamow peaks for  $T \approx 2.2$  GK (core oxygen burning) and  $T \approx 3.6$  GK (explosive oxygen burning). The solid line shows the fitted total  $S$ -factor adopted by Caughlan and Fowler (1988).



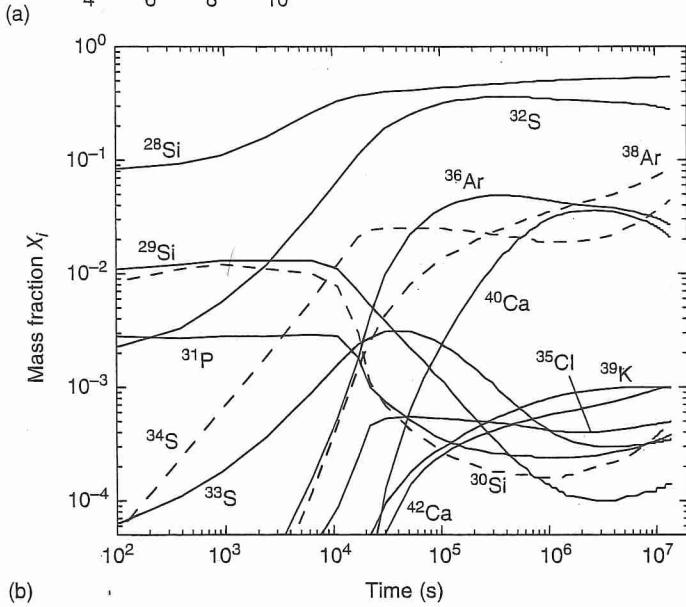
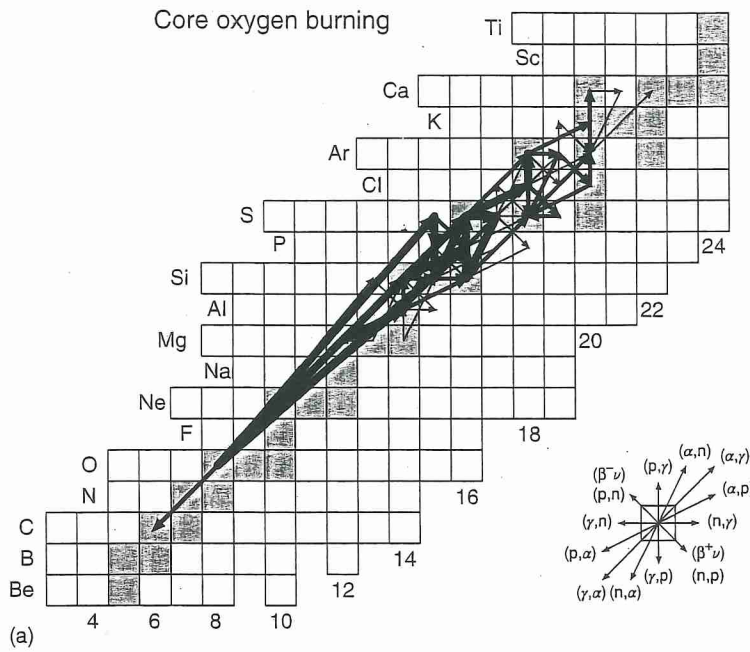


**Figure 5.32** (a) Time-integrated net abundance flows, and (b) abundance evolutions for a constant temperature and density of  $T = 2.2$  GK and  $\rho = 3 \times 10^6$  g/cm<sup>3</sup>, respectively. Such conditions are typical of core oxygen burning in stars with an initial mass of  $M = 25 M_{\odot}$  and with initial solar metallicity. The reaction network is solved numerically until the oxygen fuel is exhausted ( $X_{16O} < 0.001$  after  $\approx 162$  d). The arrows, shaded squares, and key in the top part have the same meaning as in Figure 5.26. The  $^{24}\text{Mg}(\alpha,\gamma)^{28}\text{Si}$  reaction is obscured by  $^{16}\text{O}(^{16}\text{O},\alpha)^{28}\text{Si}$  in part (a).

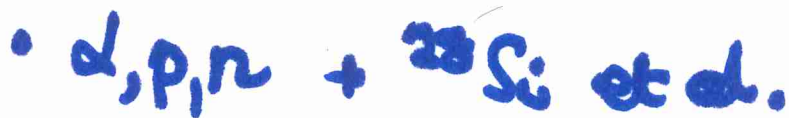
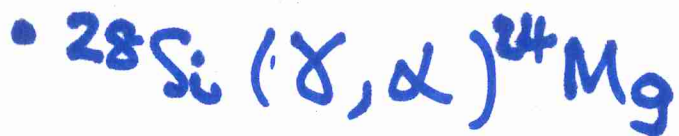


# SILICON BURNING - MASSIVE STARS

- COULOMB BARRIER !




NO!



→ Quasi-stat. eq. CLUSTERS

→ TWO at  $Z=20$  boundary



THE END OF HYDROSTATIC  
BURNING

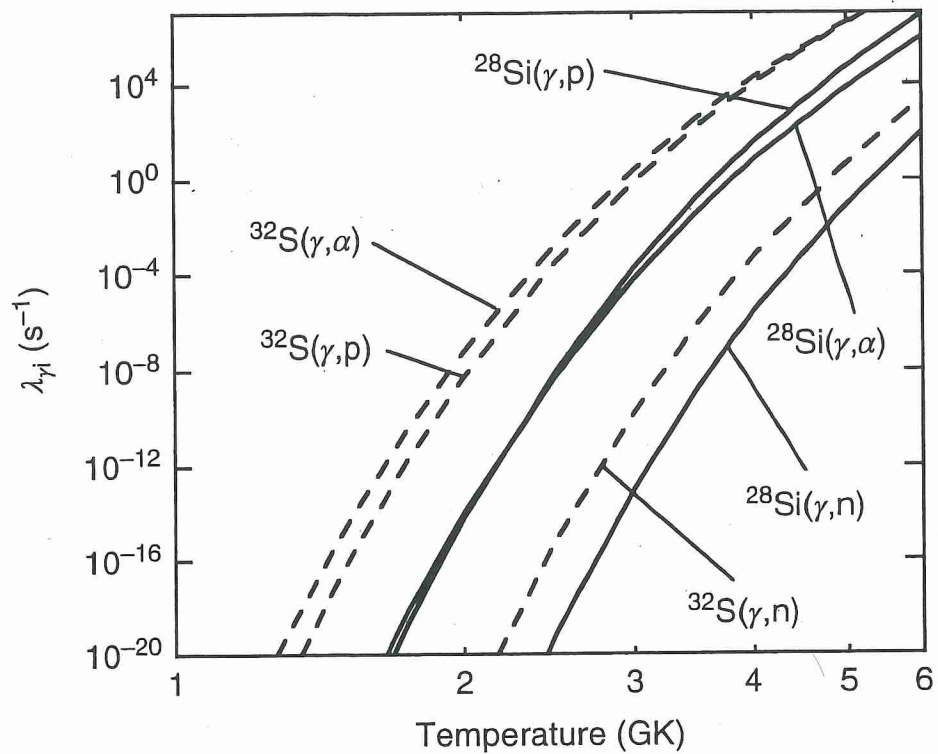


**Figure 5.33** Decay constants for the photodisintegrations of  $^{28}\text{Si}$  (solid lines) and  $^{32}\text{S}$  (dashed lines) versus temperature. The curves are calculated from the rates of the corresponding forward reactions.

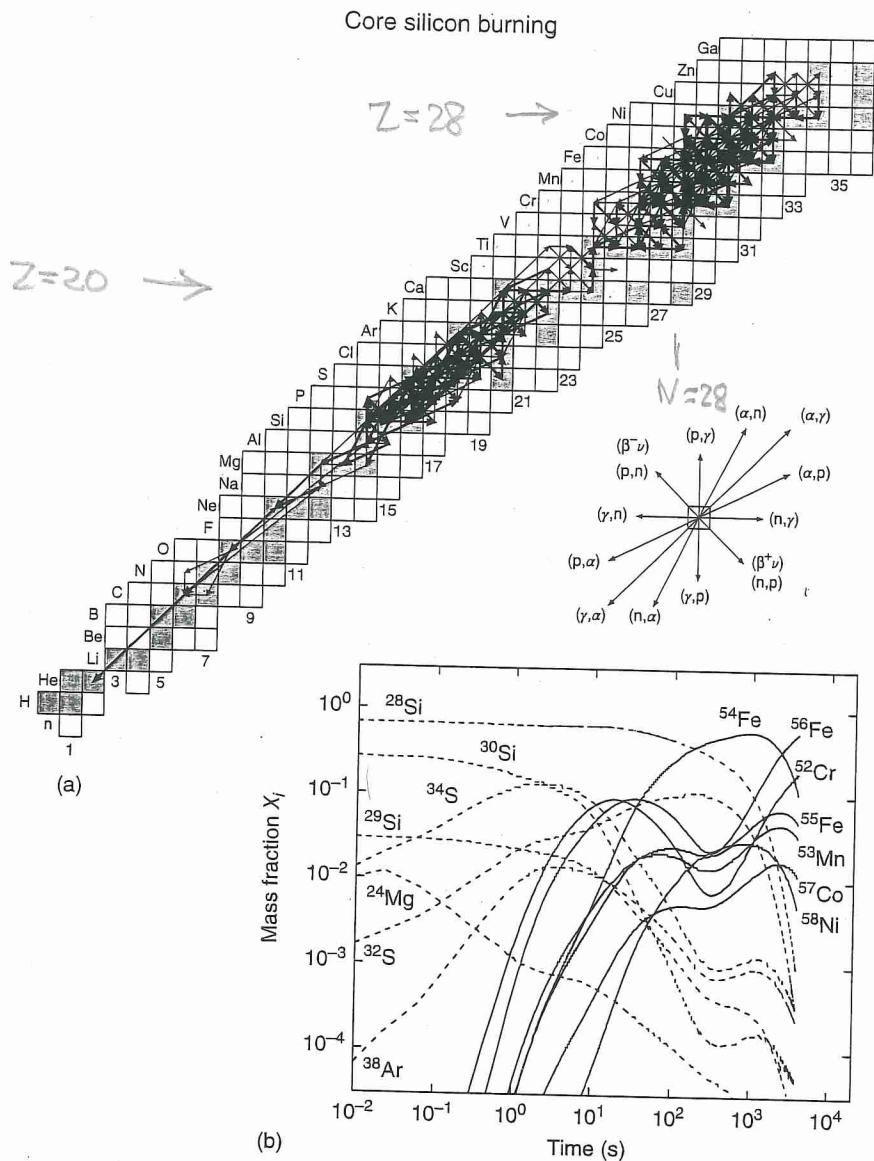


**Figure 5.34** (a) Time-integrated net abundance flows, and (b) abundance evolutions for a constant temperature and density of  $T = 3.6$  GK and  $\rho = 3 \times 10^7$  g/cm<sup>3</sup>, respectively. Such conditions are typical of core silicon burning in stars with an initial mass of  $M = 25 M_{\odot}$  and with initial solar metallicity. The reaction network is solved numerically until the silicon fuel is exhausted ( $X_{28\text{Si}} < 0.001$  after  $\approx 4000$  s). Abundance

flows are represented by arrows of three thicknesses: thick, intermediate and thin arrows show flows of  $F_{ij}^{\text{max}} \geq F_{ij} > 10^{-2} F_{ij}^{\text{max}}$ ,  $10^{-2} F_{ij}^{\text{max}} \geq F_{ij} > 10^{-4} F_{ij}^{\text{max}}$  and  $10^{-4} F_{ij}^{\text{max}} \geq F_{ij} > 10^{-5} F_{ij}^{\text{max}}$ , respectively, where  $F_{ij}^{\text{max}}$  corresponds to the reaction with the maximum flow. The abundance flows in part (a) show the existence of two quasi-equilibrium clusters in the  $A = 25\text{--}40$  and  $A = 46\text{--}64$  mass ranges.

56Fe

$$T = 3.6 \text{ GK}, \rho = 3 \times 10^7 \text{ g/cm}^3, t = 4.0 \times 10^3 \text{ s}$$

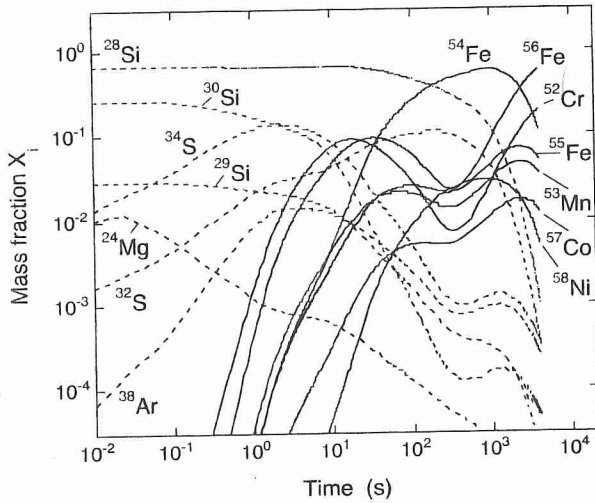
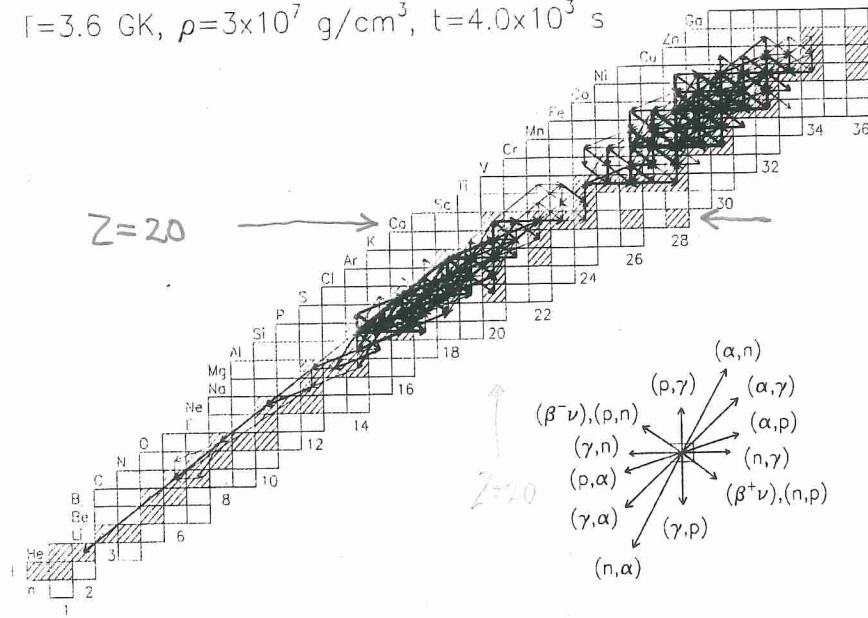


**Fig. 5.52** Time-integrated net abundance flows (top) and abundance evolutions (bottom) for a constant temperature and density of  $T = 3.6 \text{ GK}$  and  $\rho = 3 \times 10^7 \text{ g/cm}^3$ , respectively. Such conditions are typical of core silicon burning in stars with an initial mass of  $M = 25 M_{\odot}$ , and with initial solar metallicity. The reaction network is solved numerically

until the silicon fuel is exhausted ( $X_{^{28}\text{Si}} < 0.001$  after  $\approx 4000 \text{ s}$ ). The arrows in the top part have the same meaning as in Fig. 5.44. The abundance flows in the top part of the figure reflect the existence of two quasiequilibrium clusters in the  $A = 25-40$  and  $A = 46-64$  mass ranges.

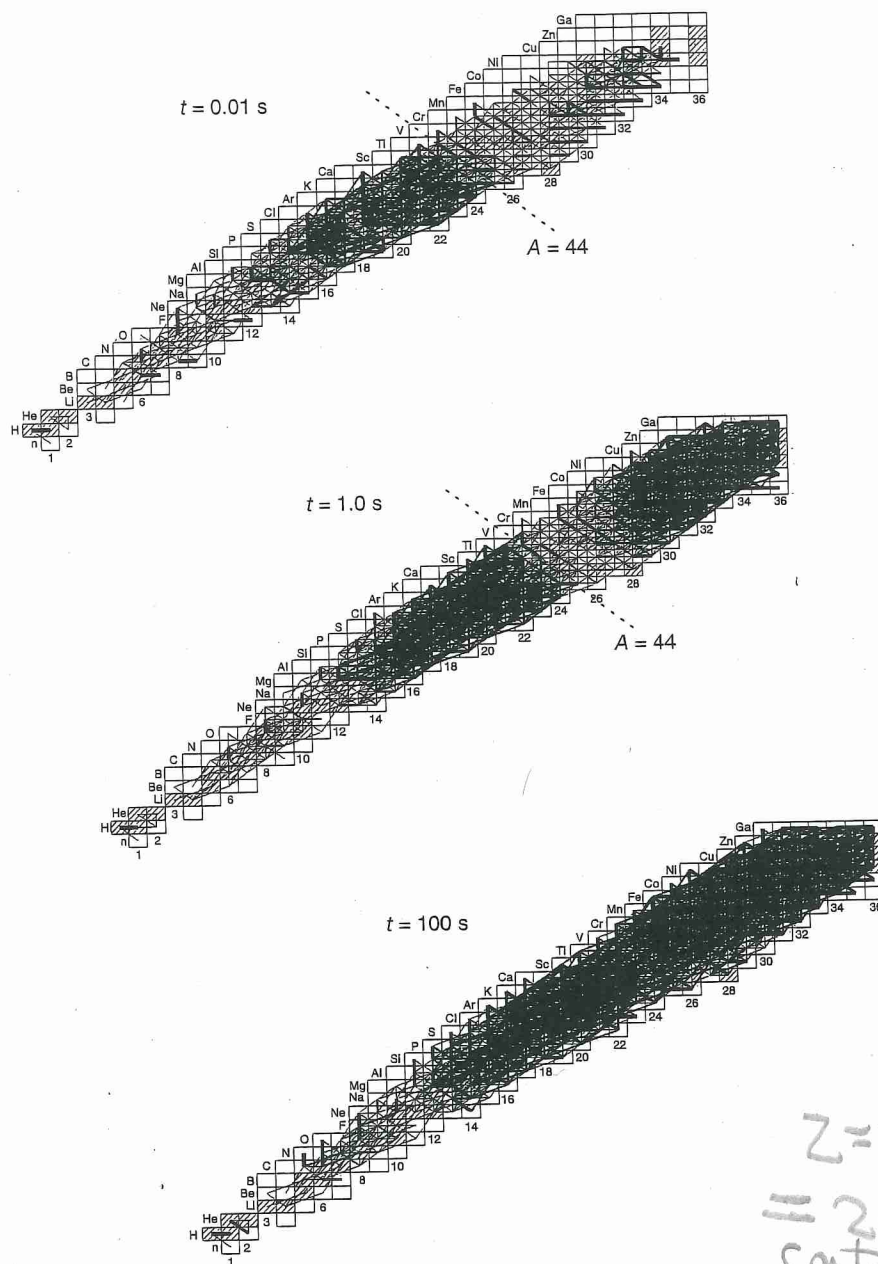


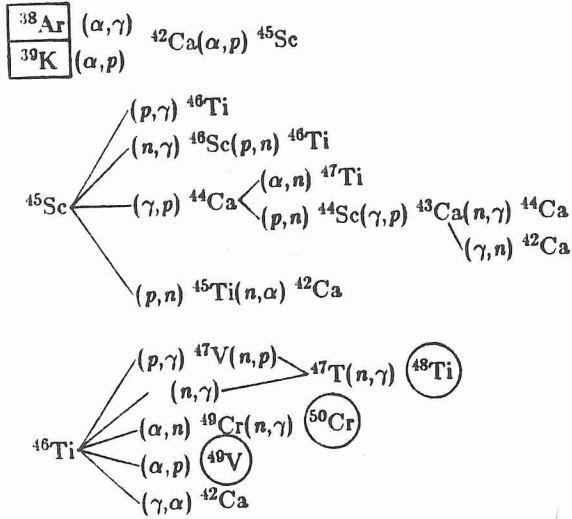
Figure 5.35 Normalized net abundance flows,  $\phi_{ij} \equiv |r_{i \rightarrow j} - r_{j \rightarrow i}| / \max(r_{i \rightarrow j}, r_{j \rightarrow i})$ , at three different times ( $t = 0.01$  s, 1 s, 100 s) for the same reaction network calculation that is shown in Figure 5.34. In each panel, the thick lines show flows with  $\phi_{ij} \leq 0.01$  (approximate equilibrium), those

of intermediate thickness represent flows with  $0.01 < \phi_{ij} \leq 0.1$ , and the thin lines correspond to flows with  $0.1 < \phi_{ij} \leq 1$  (no equilibrium). The flows  $\phi_{ij}$  are not integrated over time, but provide instead a snapshot for the evolution of quasi-equilibrium clusters during the nuclear burning.

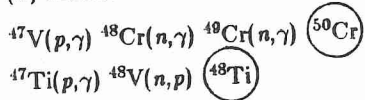
ESSENTIALLY ALL  $> 24$  Mg IN  
QUASI-EQ.

Table 11.7  
Reaction Links between the Two QSE-Groups in Si-Burning

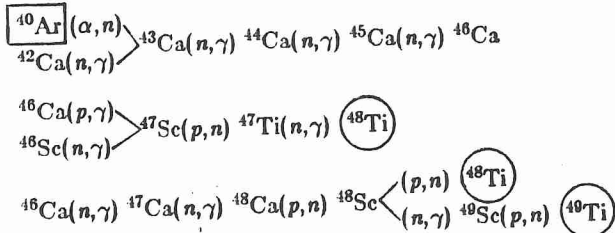
(a) basic reactions



(b) additional reactions in high temperature burning



(c) important reactions in low temperature burning



members of the first QSE group

members of the second QSE group

# OVERVIEW OF MASSIVE STAR HYDROSTATIC BURNING.

— O burning products  
Si

→ LARGELY MODIFIED  
IN SN EXPLOSION

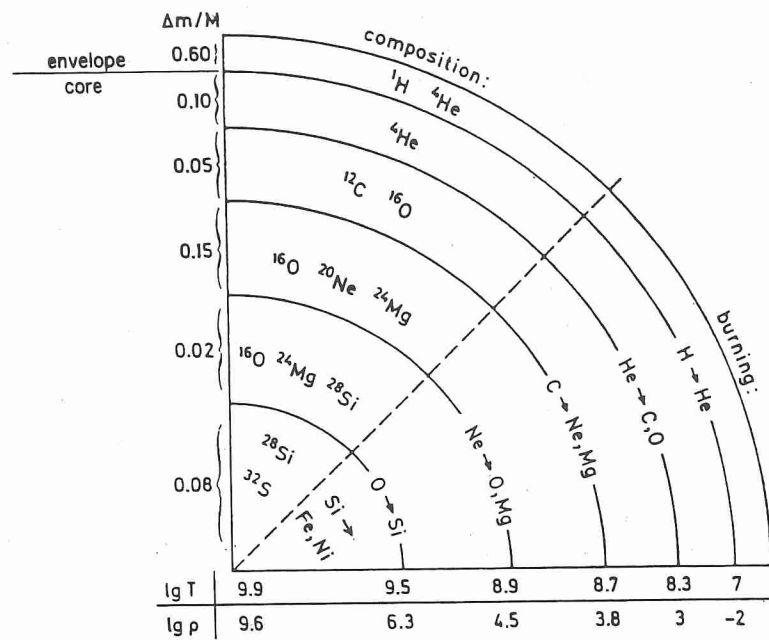


**Fig. 5.9.** Schematic illustration (not to scale) of the 'onion-skin' structure in the interior of a highly evolved massive star ( $25 M_{\odot}$ ). Numbers along the vertical axis show some typical values of the mass fraction, while those along the horizontal axis indicate temperatures and densities ( $\text{g cm}^{-3}$ ). Adapted from Kippenhahn and Weigert (1990).



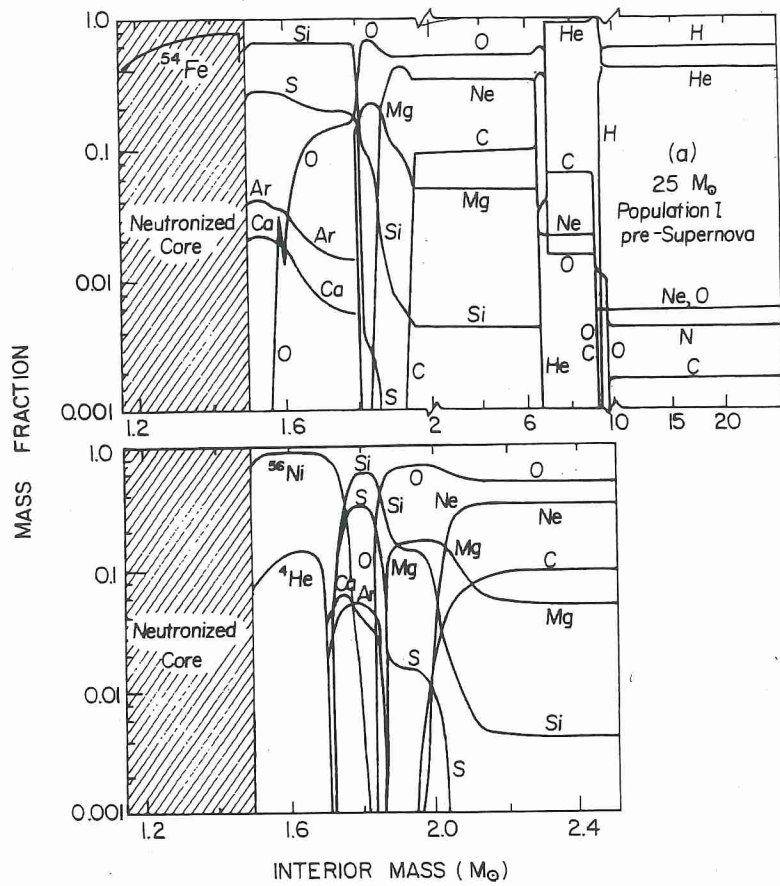


**Fig. 5.10.** Upper panel: chemical profile of a  $25 M_{\odot}$  star immediately before core collapse. (Note change in horizontal scale at  $2 M_{\odot}$ .) Lower panel: the same, after modification by explosive nucleosynthesis in a supernova outburst. The amount of  $^{56}\text{Ni}$  (which later decays to  $^{56}\text{Fe}$ ) ejected depends on the mass cut, somewhere in the  $^{28}\text{Si} \rightarrow ^{56}\text{Ni}$  zone, and is uncertain by a factor of 2 or so. Adapted from Woosley and Weaver (1982).

**Table 4.1** Burning stages of a  $20 M_{\odot}$  star

Fuel	$\rho_c$ ( $\text{g/cm}^3$ )	$T_c$ ( $10^9$ K)	$\tau$ (year)	$L_{\text{phot}}$ ( $\text{erg/s}$ )
Hydrogen	5.6(0)	0.04	1.0(7)	2.7(38)
Helium	9.4(2)	0.19	9.5(5)	5.3(38)
Carbon	2.7(5)	0.81	3.0(2)	4.3(38)
Neon	4.0(6)	1.70	3.8(-1)	4.4(38)
Oxygen	6.0(6)	2.10	5.0(-1)	4.4(38)
Silicon	4.9(7)	3.70	2 days	4.4(38)

# THE NEUTRON EXCESS, $\eta$

• AFTER Si-BURNING,  
CORE IMPLODES

→ NEUTRON STAR or BLACK HOLE

→ EXPLOSIVE N' SYNTHESIS  
& SN EJECTA

→ BRIEF EPISODE

$p \rightleftharpoons n$  conversion inhibited

PRODUCTS OF ENS determined  
partly by  $N(p)$  and  $N(n)$  at  
onset

$$N(p) = \sum N_i Z_i$$

$$N(n) = \sum N_i (A_i - Z_i)$$

$$N(\text{tot}) = N(p) + N(n) = \sum N_i A_i$$

$$\eta = \frac{N(n) - N(p)}{N(n) + N(p)}$$

$$= \frac{\sum N_i (A_i - 2Z_i)}{\sum N_i A_i}$$

with  $X_i = \frac{N_i A_i}{\sum N_i A_i}$  (nuclear fraction)

$$= \sum \frac{X_i}{A_i} (A_i - 2Z_i)$$

$$\text{and } Y_i = \frac{X_i}{A_i} = \frac{N_i}{\sum N_i A_i} = \frac{N_i}{N_{\text{tot}}}$$

= mole fraction of  $i$

BY DEFINITION:  $\eta = -1$  to  $+1$

ALSO,  $Y_e$  = ELECTRON FRACTION

$$= \frac{N_p}{N_p + N_n} = \frac{1-x}{2}$$

3) EVOLUTION IN HYDROSTATIC  
BURNING (Fig 11.9 THIELEMANN  
& ARNETT (1985))

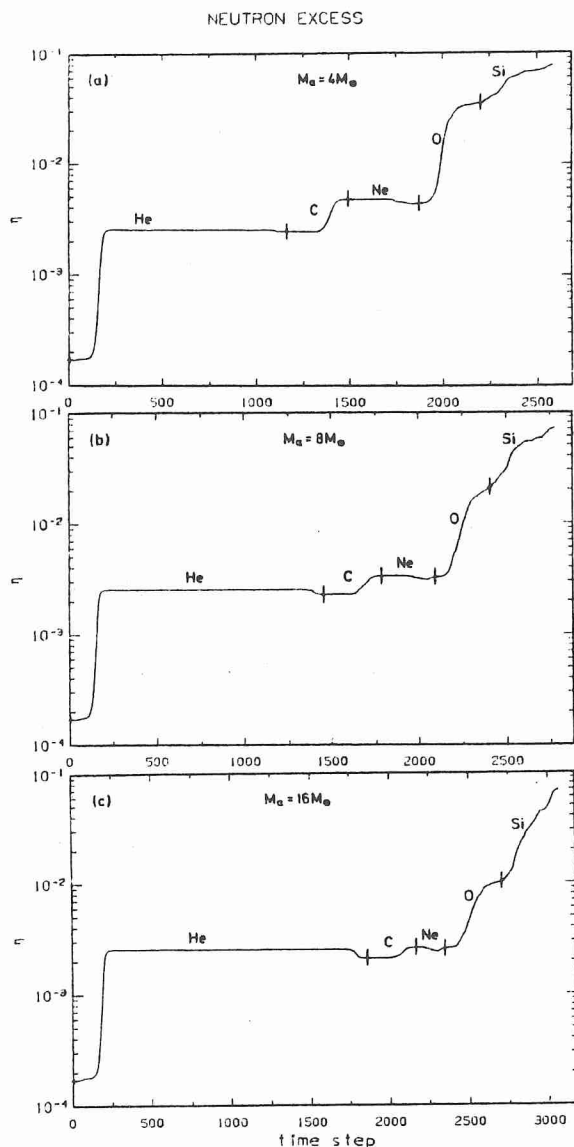


Fig. 11.9. The evolution of the neutron excess  $\eta$  during all evolutionary phases.  $\eta = \sum_i (N_i - Z_i) Y_i$  is only changed by  $\beta$ -decays or electron captures on nuclei. The increase during He-burning is due to the reaction sequence  $^{14}\text{N}(\alpha, \gamma) ^{18}\text{F}(\beta^+) ^{18}\text{O}(\alpha, \gamma) ^{22}\text{Ne}$  in all given cases. Further details are discussed in the text. The most pronounced differences are: (i) for low temperature C-burning the reaction sequence  $^{12}\text{C}(p, \gamma) ^{13}\text{N}(\beta^+) ^{13}\text{C}(\alpha, n) ^{16}\text{O}$  leads to a strong increase of  $\eta$ , (ii) under low temperature and high density conditions, electron capture on nuclei occur even in O-burning and cause a strong increase of  $\eta$ .

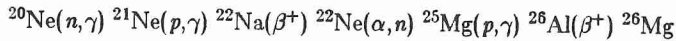
### 11.8.2 Neutron Excess $\eta$

Although a few reactions might accurately describe the main energy generation in a specific burning stage,  $\eta$  reflects the subtle details and small abundances of certain nuclei on the scale of  $10^{-2}$  in mass. Nonetheless it is important to the nucleosynthesis yields and the late burning stages in which small changes in the electron abundance  $Y_e$  have large effects on the dynamic behavior of the final core collapse.

The evolution for different He-cores can be seen in figure 11.9. The main burning products of H-burning are  ${}^4\text{He}$  and  ${}^{14}\text{N}$ , both nuclei with equal proton and neutron numbers. Therefore  $\eta$  starts at a very low level, close to  $10^{-4}$ . In He-burning the main increase is due to the  $\beta^+$ -decay in the reaction sequence  ${}^{14}\text{N}(\alpha, \gamma) {}^{18}\text{F}(\beta^+) {}^{18}\text{O}(\alpha, \gamma) {}^{22}\text{Ne}[(\alpha, n) {}^{25}\text{Mg}]$  of a nucleus with an abundance of the order  $10^{-3}$ . This is almost identical for all three initial He-core masses, but the neutron production via  ${}^{22}\text{Ne}(\alpha, n) {}^{25}\text{Mg}$  is temperature dependent and

most effective for more massive stars. The  $\beta$ -decays during  $s$ -processing decrease  $\eta$ , and consequently this effect is bigger for  $M_\alpha = 16 M_\odot$ .

In C-burning an  $\eta$ -enhancement generally occurs only via the low flux reaction sequence



(see table 11.4) which leads to a small enhancement in the case of  $M_\alpha = 16 M_\odot$ . For low temperature, high density C-burning, the reaction sequence  ${}^{12}\text{C}(p, \gamma) {}^{13}\text{N}(\beta^+) {}^{13}\text{C}(\alpha, n) {}^{16}\text{O}$  (which also supports  $s$ -processing) is effective and an increase of  $\eta$  by more than a factor of 2 is achieved for  $M_\alpha = 4 M_\odot$ . The neutron excess is little affected by Ne-burning. In O-burning one of the outgoing channels of the  ${}^{16}\text{O} + {}^{16}\text{O}$  fusion reaction,  ${}^{16}\text{O}({}^{16}\text{O}, n) {}^{31}\text{S}$ , leaves an unstable nucleus which decays by  $\beta^+$ -decay and again leads to an increase of  $\eta$ . Electron capture on nuclei is also effective during O-burning of lower mass stars ( $M_\alpha = 4 M_\odot$ ), and the strongest increase of  $\eta$  (by a factor of 8) is for  $M_\alpha = 4 M_\odot$ .

During Si-burning, electron capture is important for all He-core masses and most effective in heavier cores (see figure 11.8). Therefore the three cases almost converge to a value between 6 and  $8 \times 10^{-2}$  after  ${}^{28}\text{Si}$  is depleted to less than 1%.

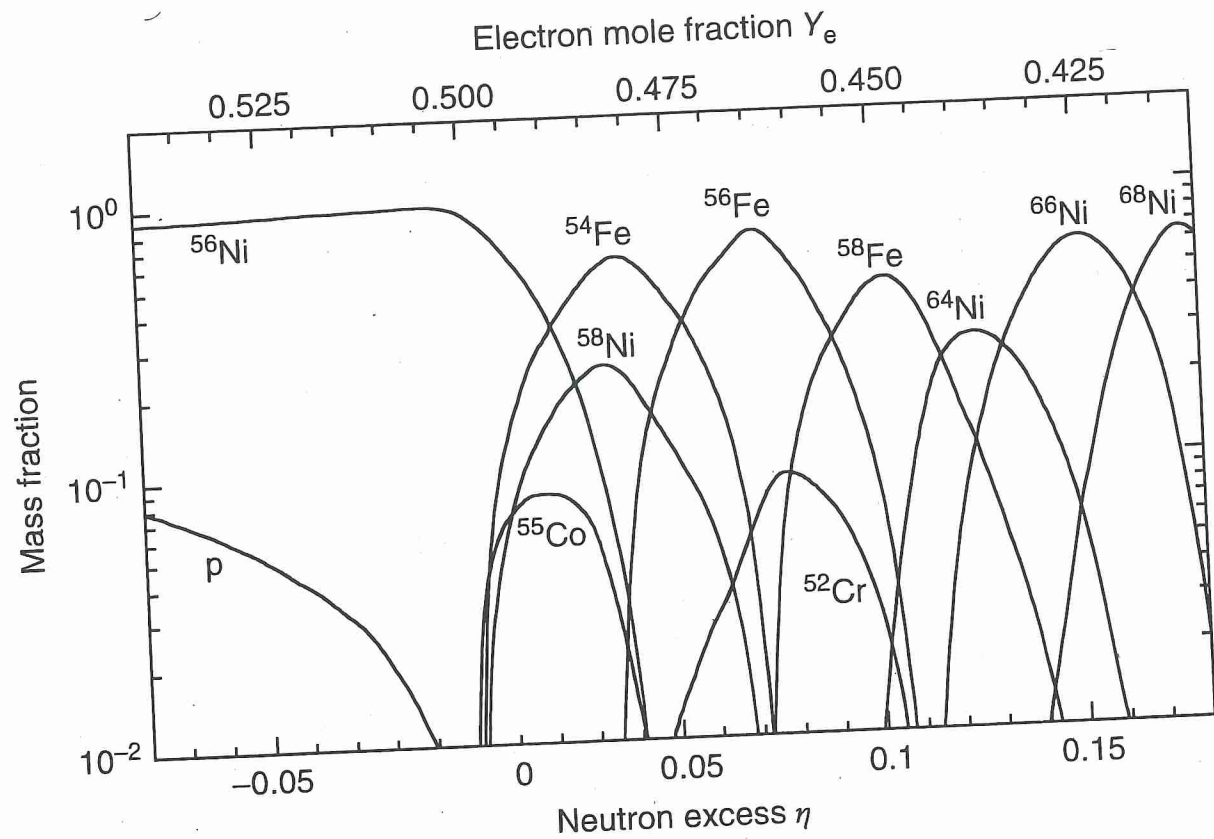


**Figure 5.39** Abundances of the dominant species versus neutron excess parameter  $\eta$  (or electron mole fraction  $Y_e$ ) in a nuclear statistical equilibrium composition at

$T = 3.5$  GK and  $\rho = 10^7$  g/cm<sup>3</sup>. The abundances on either side of  $\eta = 0$  ( $Y_e = 0.5$ ) show a different behavior. (Courtesy of Ivo Seitenzahl.)



## EXPLOSIVE H-BURNING

• HOT pp vs HOT CNO?

pp - opening step is a weak interaction

∴ v. slow / too slow to occur in explosions with  $\tau \sim$  a few s to few yrs

→ existing  ${}^2\text{H}$  &  ${}^3\text{He}$  could lead to  ${}^{12}\text{C}$  via p-captures but TOO LITTLE  ${}^2\text{H}$  &  ${}^3\text{He}$  to be significant consumer of protons